

Self-assembly in a near-frictionless granular material: conformational structures and transitions in uniaxial cyclic compression of hydrogel spheres

David M. Walker,^a Antoinette Tordesillas,^{*a,b} Nicolas Brodu,^{c,d} Joshua A. Dijksman,^{c,e} Robert P. Behringer^c and Gary Froyland^f

Received Xth XXXXXXXXXXXX 20XX, Accepted Xth XXXXXXXXXXXX 20XX

First published on the web Xth XXXXXXXXXXXX 200X

DOI: 10.1039/b000000x

We use a Markov transition matrix-based analysis to explore the structures and structural transitions in a three-dimensional assembly of hydrogel spheres under cyclic uniaxial compression. We apply these methods on experimental data obtained from a packing of nearly frictionless hydrogel balls. This allows an exploration of the emergence and evolution of mesoscale internal structures — a key micromechanical property that governs self-assembly and self-organization in dense granular media. To probe the mesoscopic force network structure, we consider two structural state spaces: (i) a particle and its contacting neighbours, and (ii) a particle's local minimal cycle topology summarized by a cycle vector. In both spaces, our analysis of the transition dynamics reveals which structures and which sets of structures are most prevalent and most likely to transform into each other during the compression/decompression of the material. In compressed states, structures rich in 3-cycle or triangle topologies form in abundance. In contrast, in uncompressed states, transitions comprising poorly-connected structures are dominant. An almost-invariant transition set within the cycle vector space is discovered that identifies an intermediate set of structures crucial to the material's transition from weakly jammed to strongly jammed, and vice versa. Preferred transition pathways are also highlighted and discussed with respect to thermo-micro-mechanical constitutive formulations.

1 Introduction

The physics of granular materials is of great import to science and engineering¹. Packings of granular materials come in many varieties: pharmaceutical pills, roads and pavement, ceramics, chemical powders, fault gouge, fertilizers, geotextiles, proppants, grains, M&Ms, soil, rock and mineral ores all involve examples from the broad spectrum of granular materials. A full and deep understanding of granular materials, in particular, how they respond to mechanical stimuli is thus crucial to improved manufacturing processes², increased energy efficiency and performance of novel designs³ of engineered granular materials⁴, risk assessment and disaster mitigation in both industry⁵ and the natural world^{6,7}. When subject to applied loads (e.g., shearing, compression etc.), the

constituent particles in the material self-assemble into mesoscopic structures⁸ whose mechanical properties enable the material to mimic behaviour at the macroscopic scale that is solid-like, or liquid-like, or both^{9,10}. A recent study of the process of self-organization in a two-dimensional photoelastic disk assembly under shear has laid bare some underlying mechanisms behind such diverse behaviour at the macroscopic level¹¹. In that study, we uncovered magic-number like behaviour at the mesoscale, akin to molecular self-assembly¹¹: in particular, a complex interplay between forces and contact topology drove grains to rearrange and form structurally stable conformations at the scale of a grain and its first ring of neighbours. We found these favoured conformations to reside in distinct preferred stability bands (i.e., very narrow range of stability states), with favoured conformational transitions to be those where the loss and gain of contacts confine resultant conformations to the same stability band: very high stability barriers exist to prevent conformational transitions that incurs a jump from one stability band to another. In this study, we take the first steps toward discovering the details of self-assembly in the context of favoured mesoscale structures and structural transitions that emerge in the jammed (solid-like) versus unjammed (liquid-like) regimes of the phase space of three-dimensional granular matter^{12,13}. The expected out-

^a Department of Mathematics and Statistics, University of Melbourne, Parkville, VIC 3010 Australia. Fax: 61 3 8344 4599; E-mail: atordes@unimelb.edu.au

^b School of Earth Sciences, University of Melbourne, Parkville, VIC 3010 Australia.

^c Department of Physics, Duke University, Durham, NC 27708 USA.

^d INRIA, 200 avenue de la Vieille Tour, 33405 Talence, France.

^e Department of Physical Chemistry and Colloid Science, Wageningen University, PO Box 8083, 6700EK Wageningen, The Netherlands.

^f School of Mathematics and Statistics, University of New South Wales, Sydney, NSW 2052 Australia.

comes are multifaceted, both from the perspective of fundamental research and in practical applications. Knowledge of the most prevalent structures and their transitions in the different regimes of the phase space of a granular material provides specific insights into what key structures and associated rearrangement pathways should be considered in thermo-micro-mechanical constitutive formulations, which are based on so-called internal variables (e.g. non-affine deformation¹⁴ or damage-healing tensors¹⁵, computed from loss-gain of contacts within mesoscopic structures). Other approaches have also been proposed. In Chai *et al.*¹⁶, the contact forces in chains of grains within rough, frictional granular materials in a jammed configuration was studied with respect to pressure to reveal universal scaling properties. Investigating the dynamics of self-assembly and self-organization in a three-dimensional granular material may shed light on possible underpinning mechanisms responsible for the emergence of such scaling laws. We also envisage a range of practical applications. These include the design of granular materials with tailor-made properties (e.g., 3D printed particulate systems) as well as the design of additives in the form of granules admixed to a wide range of granular materials to manipulate their macroscopic behaviour under various loading conditions: additives to stabilize and strengthen road and off-road construction materials, pavement, ceramics, geopolymer composites and other geomaterials, and additives to enhance flowability of manufactured materials during handling and storage while at the same time enabling them to efficiently respond to small changes in mechanical stimuli (e.g., from a weakly jammed state, readily self-compact for storage and transport purposes).

There are many limiting factors to obtaining a clear understanding of self-assembly and self-organization processes in granular systems¹¹. Two key micro-mechanical properties that govern the formation of structures in the mesoscale are grain shape and friction. While many past studies have considered spherical versus non-spherical grain shapes, in numerical simulations^{17,18} and experiments¹⁹, the design and execution of a three-dimensional physical test close to frictionless conditions is less common. An additional problem is that such a test must permit a rigorous exploration of structures and their associated topologies, from both a statistical and a physical standpoint. Here we propose a tightly coordinated experimental-theoretical effort that overcomes all of these challenges. On the experimental side, we consider a three-dimensional experimental system of hydrogel spheres^{20,21} whose properties and loading protocol reduce the effects of friction and grain shape. Specifically, the assembly of hydrogels is near-frictionless with individual grains being close to spherical in shape. This allows an unprecedented opportunity to explore the evolution of contact topology in near isolation in a physical test — free from the major influences of friction and grain shape that control structural self-assembly in dense granular media. Further-

more, the experimental test involves a cyclical loading protocol across many cycles, each encompassing both jammed and unjammed macroscopic mechanical states²⁰. Within this single test, the sample is driven backwards and forwards between jammed and unjammed states, or at least strongly jammed versus weakly jammed states, thereby permitting the discovery of robust mesoscale structures that uniquely define macroscopic strength and failure of dense granular matter in these two distinct regimes of the granular phase diagram. In two dimensions, the jamming behaviour of packings of frictionless particles have been thoroughly enumerated and investigated in numerical simulations with respect to various mechanical properties^{22–25}. Reichhardt and Reichhardt²⁶ also discuss jamming in two-dimensional granular systems as well as other forms of material and matter. On the theoretical side, we employ a Markov transition matrix-based analysis²⁷, which exploits the tens of cycles to identify structures and structural transitions in the mesoscopic domain.

More specifically, we explore the structures and structural transitions observed within the cyclically compressed material using two structural state spaces at different mesoscopic scales. In the first state space, we explore the transition dynamics of structures, or conformations, formed by a particle and its contacting neighbours. The analysis follows that performed in Tordesillas *et al.*¹¹ on an assembly of two-dimensional photoelastic disks subject to reverse shear²⁸. The structures extracted in this state space typically consist of star sub-networks with some closed triangles (i.e., 3-cycles). In the second state space, we are motivated by findings in Walker *et al.*²⁹ which considers a cycle vector summarizing the local n -cycle topology of a particle. Importantly, the novelty of the cycle vector space approach is that it probes larger length scales in the packing, thereby giving even better access to the process of self-organization across multiple length scales in the meso-domain. In both structural state spaces, the Markov transition matrix analysis reveals the most prevalent states, namely, the most abundant structures, as well as sets of structures that transition amongst each other. Weakly jammed states are dominated by structures in the contact network that are distinct from those in the strongly jammed state, and we can track how the sets of structures switch roles during compression versus decompression.

The ability to enumerate all of the structures, at a specific length scale, a packing of particles experience is important for the development of constitutive models of deforming granular media. For example, if all structures in a given system are known, then the frequency with which specific structures occur can be accurately measured. This knowledge provides the building block structures with which to base a micro-mechanical Cosserat continuum analysis^{14,15,30}. Further, the ability to identify all structures and to classify their internal rearrangements across a strain step gives a frequency,

i.e. a way to quantify how often specific structures transform into other structures. This is precisely the information required for the aforementioned thermo-micro-mechanical internal variable theory^{14,15,30}. This study provides this information across different length scales for a physical system close to the frictionless limit.

The rest of this paper is organized as follows. In Sec. 2 we briefly describe the hydrogel experimental system, and discuss the two structural state spaces and methods used to quantitatively study this system. In Sec. 3 we report on the most prevalent mesoscopic structures and discuss the character of their transitions sets with respect to the macroscopic jammed and unjammed mechanical states. We close the paper with a brief summary of our findings and their potential implications for manipulation of existing, as well as design of novel, granular materials.

2 The experiment and methods of analysis

2.1 System

The granular material we use is a packing of ~ 500 hydrogel beads^{31,32} that are approximately spherical with a typical mean diameter of $\sim 2\text{cm}$. They are submersed in a solution of water and polyvinylpyrrolidone, such that the index of refraction of the particles is well matched to the solution, to allow for refractive index matched tomography³³. The particles are almost density matched with the solvent, and have a buoyancy corrected density of less than $10\text{kg}/\text{m}^3$. The solvent-particle mass is completely transparent; in order to obtain contrast, the particles are dyed with a hydrophobic fluorescent dye (Nile Blue 690) that can be excited with a laser sheet. This laser sheet (Lasiris SNF 635nm, 25mW) is mounted on a fast stage; the light sheet can be moved to illuminate the entire sample slice-by-slice. A fast camera (Basler ava1000-120) equipped with lens and long pass filter is mounted on the same stage to record the fluorescent cross sections that the laser sheet illuminates, similar in design to Lorincz and Schall³⁴. A typical volume is imaged with 360 slices.

We cyclically and uniaxially compress the granular material in a rectangular box by confining it, from the top, with a stage-controlled piston. This top piston plate is made of a 6mm thick perforated sheet; at all times, water can freely flow in and out of the packing, making the pore pressure essentially zero. The top piston is attached to a linear stage (Newport MTM250) controlled by a closed loop controller (Newport XS4). The compression step resolution is 1 micro meter, and the compression speed is set to 0.1mm per second during experiments to reduce fluid induced shear stresses on the particles and to drive the system completely quasi-statically. The spacing between the piston plate and the walls is such that particles cannot escape confinement. While compressing/decompressing

the sample, we measure the pressure exerted on the top piston with a force sensor. The container base size is 16.5cm x 16.5cm; packing height depends on the compression level. More setup details can be found elsewhere²¹.

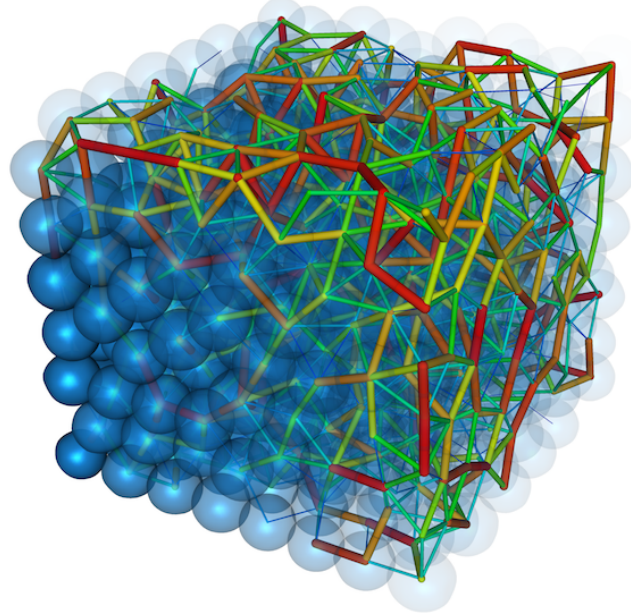


Fig. 1 A rendering of the assembly and its contact force topology. Thickness and colour of lines connecting contacting grains represent the magnitude of the contact force: thin-blue (thick-red) lines correspond to low (high) forces.

Each cycle of compression/decompressions consists of 60 small quasi-static steps (30 compressive, 30 decompressive). After each compression step, we make a complete scan of the packing and reconstruct the three-dimensional structure of the packing with image de-noising and perspective corrections. In order to obtain the contact forces, we implement custom computer algorithms that work according to the following scheme. First, we identify the boundaries of each particle, including regions of contact with another particle. This gives us information about both the centre of mass of the particles, and the locations of the particle contacts. Then, from the areas of contact, we use linear elasticity, and the measured elastic properties of the particles, to infer the contact forces. See, for example, Fig. 1 which displays a rendering of the sample and its contact force topology. Note that hydrogel contacts are slippery with a friction coefficient of $\mu \approx 0.03$, so all contact forces on the particles are normal to the contact plane. We then compute the micro-and-coarse-grained stress tensor. We have verified that this stress tensor information is consistent with independent other measures, such as the top plate force sensor measurement.

In this study, we are primarily interested in the topological structures that the hydrogel beads form through their contacts. It should be emphasized, however, that there is an experimental resolution limit on detection of weak forces and hence, contacts. In particular, for the least compressed time steps of the cyclic loading we will miss (possibly many) weak links and consequently undercount contacts. Conformations observed with fewer contacts during decompression may in actuality be more densely connected but it is beyond current technology to be more accurate. This issue should be borne in mind when we report on the prevalence of loosely connected conformations. Furthermore, we only perform a topological analysis of the structural topology. We do not distinguish between a structure possessing many so-called strong force contacts, say above average in magnitude, from the same structure possessing many weak force contacts, i.e., below average magnitude. We reserve for a future analysis incorporation of the measured contact forces to distinguish such differences.

2.2 Structures

The constituent parts of a granular medium, i.e., the solid particles, self-assemble to form various sub-structures within the medium. The type and form of these structures has important consequences for the stability and load-bearing capacity of a granular material⁹. The identification of structures within a granular material is a greater challenge in three dimensions than in two-dimensional simulations and experiments. The mathematical modelling of the evolving dynamics of such structures provides a further challenge.

A useful topological representation of a granular material from which sub-structures can be identified is the contact network^{35,36}. Here each particle and its contacts can be identified so that the entire granular assembly can be represented by a complex network. A complex network consists of a collection of nodes which are connected by links. This information can be usefully summarized with a matrix whose elements a_{ij} are either zero or one; we call this matrix the adjacency matrix. $a_{ij} = 1$ corresponds to a link (contact) between nodes (particles) i and j . The structure of the network can be summarized by many properties across different scales. For example, locally, one can count the number of links associated to each node (i.e., the degree), or the number of contacting neighbours of a node that themselves are in contact with each other (i.e., triangular structures). Specifically, when a complex network is represented by an adjacency matrix the degree of a node i is given by

$$k_i = \sum_{j=1}^n a_{ij} \quad (1)$$

where a_{ij} is the $(ij)^{th}$ element of the $n \times n$ adjacency matrix for n particles. We can summarize an aspect of the network and

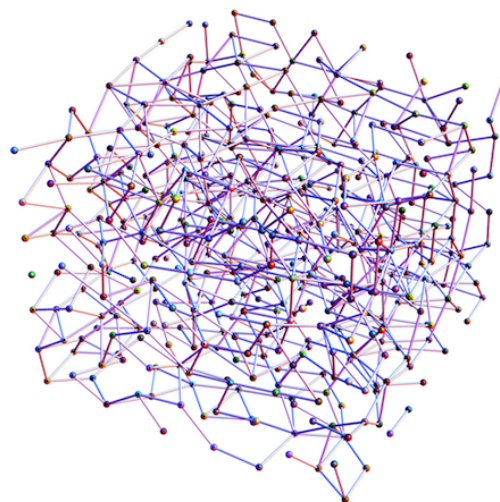


Fig. 2 Example of an observed contact network when hydrogels are in a weakly jammed configuration.

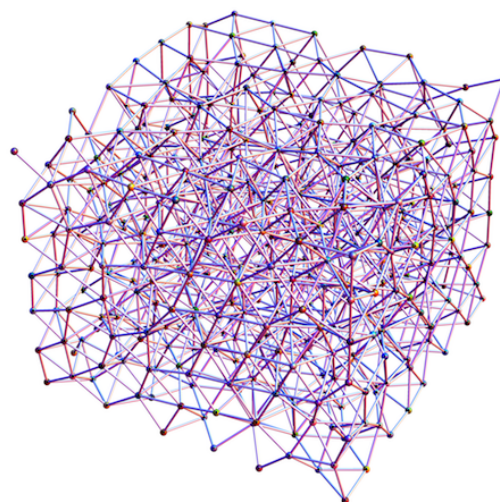


Fig. 3 Example of an observed contact network when hydrogels are in a strongly jammed configuration.

consequently the assembly by examining the average value of k_i across all particles. The clustering coefficient reflects the extent of local connectivity by quantifying the number of triangles associated with a node i ³⁷. One measure is to quantify the ratio of observed triangles to the maximum number possible given a node's degree, i.e., the clustering coefficient of a node i is

$$c_i = \Delta_i / \binom{k_i}{2} \quad (2)$$

where k_i is as in Eq. 1 and Δ_i is the number of triangles containing node i . As for degree, we can summarize this aspect of a complex network by averaging c_i across all particles to obtain \bar{c} . Each clustering coefficient and the global average \bar{c} lie in the range $[0, 1]$. The higher the value the more densely connected the local and global topology.

In the current experiment the assembly of hydrogels are loaded cyclically through decompression and compression. When the assembly is completely decompressed, it is only weakly jammed from a small hydrostatic pressure gradient; when it is compressed, we call the state "strongly jammed". We show in Fig. 2 an example of the contact network of a weakly jammed configuration. In Fig. 3 a contact network of a strongly jammed configuration is shown. Comparing the two contact networks we see fewer connections in the weakly jammed configuration, likely due to residual gravitational loading, as well as some isolated small sub-networks and fewer closed paths. However, these may be fewer than observed due to experimental error causing undercounting of contacts. In contrast, the contact network of the strongly jammed configuration exhibits many more connections forming many closed paths including numerous triangles. These two aspects are well-summarized by the average degree and average clustering coefficient of the contact networks as shown in Figs. 4. Strongly jammed configurations throughout the cyclical loading have an average degree (average number of contacts per hydrogel particle) that peaks above seven, and drops to almost three for weakly jammed configurations. Similarly, the average clustering coefficient oscillates between higher and lower values when the sample is strongly jammed and weakly jammed respectively. We seek to understand the self-assembly of such mesoscopic structures and their transition dynamics which are responsible for such macroscopic response under load.

For example, two structures that spring to mind when one considers a three-dimensional granular assembly are the tetrahedra and pyramid as shown in Figs. 5. It is a straightforward exercise to identify and enumerate instances of these structures from an adjacency matrix describing a three-dimensional contact network. Both of these small sub-structures contain many triangles. According to the clustering coefficient, if these structures are present in the assembly, we would expect their abundance to peak when the system is in strongly

jammed configurations. This is indeed the case as both tetrahedral and pyramid structures are most prevalent during strongly jammed configurations when both average degree and average clustering coefficient peak. During weakly jammed configurations these structures are less abundant and are not observed when the assembly is at its most weakly jammed. We also remark that if a strut is added to the base (square) of a pyramid then the pyramid is replaced by two tetrahedra.

The tetrahedra and pyramid are but two structures of the multitude within a three-dimensional assembly and reliably identifying and enumerating all possible structures is a challenge we have not yet overcome. However, the Johnson Solids³⁸ may be a useful starting point. We therefore take a different tack and examine the assembly at two different scales. Since structures within the assembly correspond topologically to sub-networks of the contact network, we examine two types of sub-networks: (i) those in conformations consisting of a particle and its contacting neighbours as studied in two-dimensional assemblies¹¹, and (ii) the set of (minimal) cycles a particle is a part of^{29,39,40}.

2.3 Conformations

We study a set of conformations involving particles and their contacting neighbours. These conformations can be identified by considering the sub-network formed by a node and its collection of linked neighbours. For example, if a particle has no contacting neighbours then the sub-network is the node itself. If a particle has only one contacting neighbour then the sub-network consists of the link joining the two nodes. If a particle has two contacting neighbours then there are two possible sub-networks. These are the sub-network forming an open triangle, or the sub-network forming a closed triangle topology. Continuing in this way, and without consideration of geographical constraints (i.e., particle overlap or blocking), we see that a node of degree k will have a total of $2^{k(k-1)/2}$ possible sub-networks. As the degree increases, the number of possible sub-networks can become very large. For example, for $k = 7$, there are greater than two million possibilities. In an actual realization of a granular material, the number of conformations is a lot less than the theoretical maximum number. This is because no overlap of particles is allowed. Consequently, particles can prohibit, or block, a particle's contacting neighbours from being in contact with each other. In a two-dimensional experiment of bidisperse photoelastic disks¹¹, we found only 28 distinct conformations despite the maximum observed degree being $k = 6$; greater than 32000 are possible if particle overlap is allowed. In the present hydrogel experiment, consisting of 1200 steps in a cyclic loading programme, we only observe 5473 distinct conformations, despite the maximum degree reaching $k = 14$ during a time step of loading. Our goal is to identify all possible conformations involving a

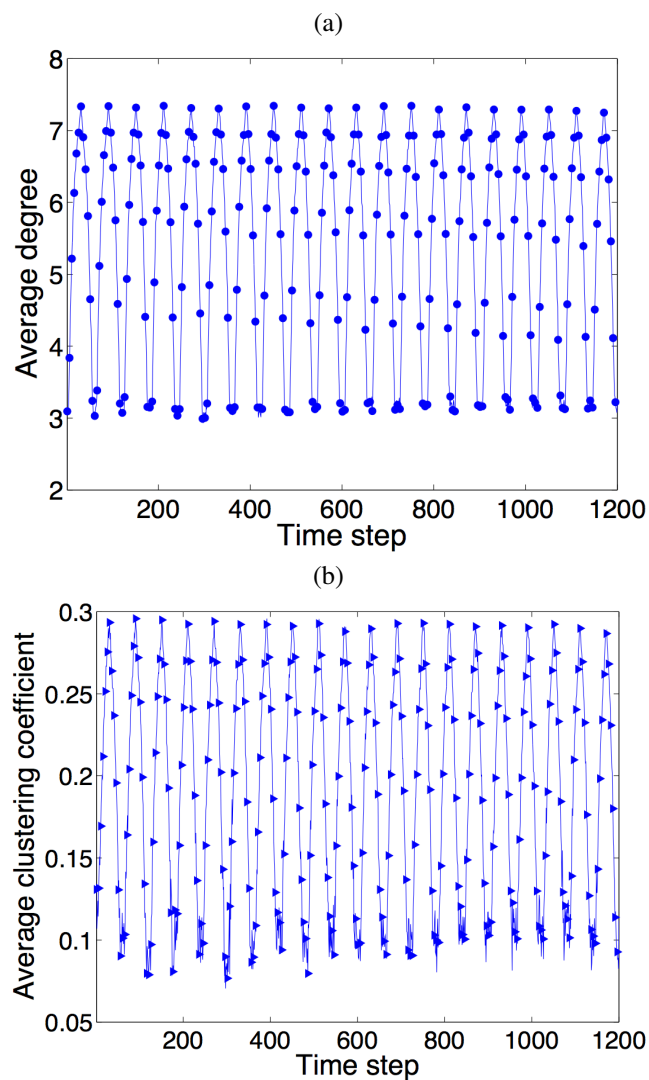


Fig. 4 Basic complex network descriptors of the hydrogel contact networks throughout cyclical loading (a) average degree, and (b) average clustering coefficient. Symbols are plotted every fifth time step for improved clarity. Peaks in both panels correspond to time steps of greatest compression, whereas troughs correspond to time steps of least compression.

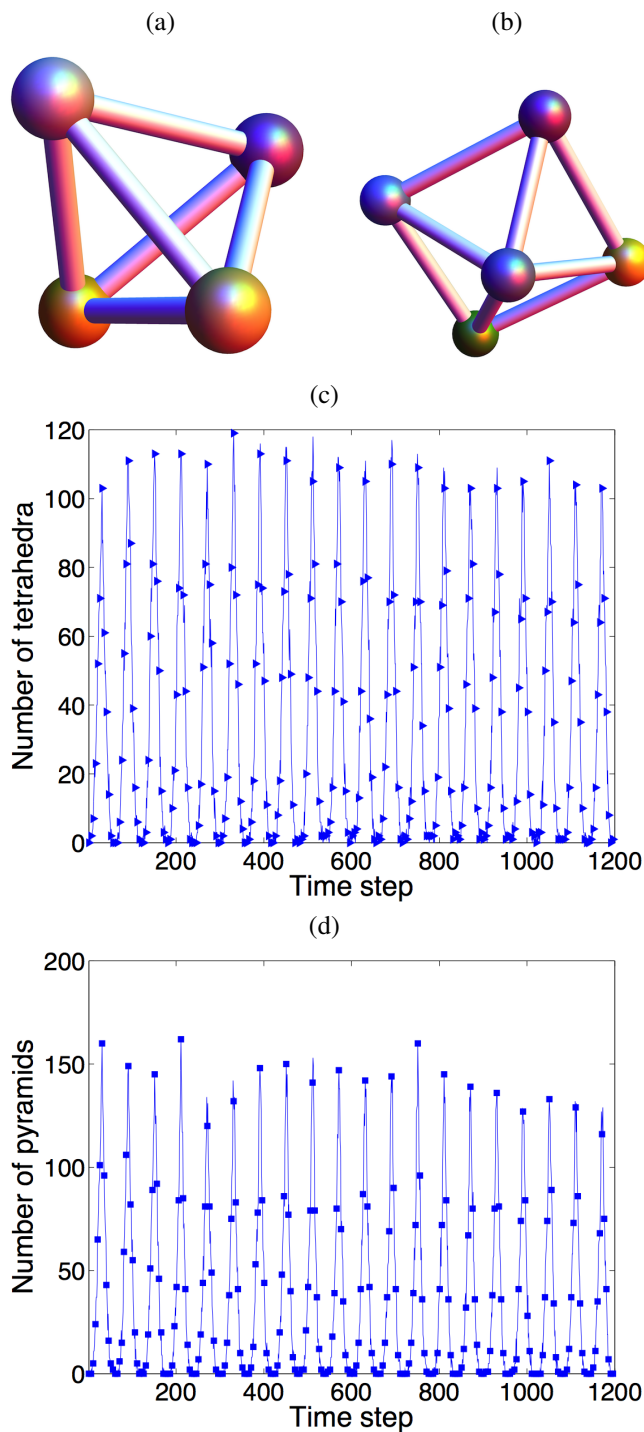


Fig. 5 Two basic three-dimensional structures and their observed instances within the hydrogel assembly throughout cyclical loading (a) Tetrahedra, (b) Pyramid, (c) Tetrahedra population, (d) Pyramid population. Symbols are plotted every fifth time step for improved clarity. Peaks in both plots correspond to greatest compression, whereas troughs correspond to least compression.

particle and its contacting particles. We treat each distinct conformation as a member of a finite state space. By tracking how each particle's local topology changes through cyclic loading, we can build a transition matrix. The properties of this matrix helps establish the most abundant conformations. Also it identifies which sets of conformations are more likely to transform into each other by forming and breaking contacts when the material moves from strongly jammed configurations to weakly jammed configurations, and vice versa. We have successfully applied this data analysis method in earlier work examining a reverse-sheared two-dimensional photoelastic disk assembly¹¹.

2.4 Cycle vector space

The conformations introduced in the preceding section consist of a particle and its local contacting topology. Contacts outside the particles' immediate influence are ignored except for those between particles which help form triangle, or 3-cycle, topologies with the central particle. The special topology of the pyramid and other such prisms can form sub-networks with $n = 4$ cycles and higher length n -cycles — self-avoiding closed paths with n links — but typically the conformations above predominately contain 3-cycles. In a granular material, the changing local n -cycle topology of a particle for $n \geq 3$ has been shown to be important with respect to possible energy dissipation mechanisms²⁹. Sub-structures involving a particle and all particles in its “cycle-of-influence” can be represented by considering a summary of the minimal cycle topology of a particle. Specifically, for a given observed time step of the deformation, each particle and its associated network node is a member of a collection of minimal n -cycles⁴⁰. We refer to any particle that is not in a cycle as a rattler: these particles are easily dealt with by considering the particle itself as a sub-structure. A summary of the n -cycle topology can be represented by a vector whose elements are a count of the number of n -cycles associated to a node. That is, at time t for a particle labelled i we construct the cycle vector

$$C_t^i = [c_0, c_3, c_4, \dots, c_n] \quad (3)$$

where c_3 corresponds to the number of 3-cycles associated with node i , c_4 is the number of 4-cycles and so on. To include particles not in any n -cycle we set $c_0 = 1$ and $c_n = 0, n \geq 3$. We note that such sub-structures necessarily include all of the previous section conformations as a subset although this is not encoded in the representation.

For example, all four of the nodes in the tetrahedral structure shown in Fig. 5 have a cycle vector given by $C^{tetra} = [0, 3, 0, \dots, 0]$. This is because each node participates in three 3-cycles. In contrast the five nodes in the pyramid structure have different cycle vectors. If we consider the four nodes involved in the pyramid base, or 4-cycle, then their cycle vectors

are given by $C_{base}^{pyramid} = [0, 2, 1, 0, \dots, 0]$. The apex node of the pyramid has a cycle vector of $C_{apex}^{pyramid} = [0, 4, 0, 0, \dots, 0]$. In practice, we set a maximal n -cycle size c_{max} and absorb any n -cycle larger than this size in the c_{max} count. Furthermore, the observed data is too sparse relative to the vast number of unique cycle vectors, meaning it is expedient, and numerically more stable in what follows, to consider a representation of these cycle vectors which forms a symbolic cycle state space. Thus, we threshold, or symbolize, the cycle vector entries to be 1 or 0 if c_n is non-zero or not. That is, there is no distinction in the cycle vectors for two particles having one and three 3-cycles respectively. The nodes of the tetrahedra thus have a symbolic cycle vector given by $s^{tetra} = [0, 1, 0, \dots, 0]$ and the pyramid's base nodes have a symbolic cycle vectors corresponding to $s_{base}^{pyramid} = [0, 1, 1, 0, \dots, 0]$. This “symbolization”, or coarse-graining, of the finite cycle vector space reduces the dimension of the cycle space from possibly thousands of different representations to hundreds. As a result the numerics are more stable but the analysis still retains the salient features of the deformation, as we are still retaining information on the presence of an n -cycle in the local topology. Since the cycle vectors account for n -cycles larger than $n = 3$, the cycle vector space encompasses a larger mesoscopic length scale than the finite conformational space. For example, by setting $c_{max} = c_{10}$ we are considering a neighbourhood of up to five particle diameters away from the central particle. If we denote the average particle diameter to be $\langle d \rangle$ then overall, throughout the experiment, we find the average distance between a central particle and its neighbours for conformations is $0.97\langle d \rangle$ compared to $1.45\langle d \rangle$ for the cycle vectors.

2.5 Transition matrix

In simulations and experiments where individual particles can be tracked, we can build up an evolution history of the sub-structures associated with each particle it is involved with. These sub-structures, or representations thereof, can be considered to form a finite state space. The changes in a particle's sub-structure yields a path through this state space. We can analyze these paths for all particles to build a transition matrix of the evolving sub-structures in the material. The key insight obtained from these concepts is that they allow us to see the preferred sub-structures that groups of particles form and the preferred changes that sub-structures undergo for a given type of loading¹¹.

We label the states of the finite state space $s_i, i = 1, \dots, N$. For conformations these s_i correspond to the distinct sub-networks formed by a particle and its contacting neighbours. For the cycle vector space these s_i correspond to the unique symbolic cycle vectors. An element M_{ij} of the transition matrix M is obtained by counting the number of times a particle observed at time t to be in state s_i is observed at time $t + 1$

to be in state s_j . The matrix M is converted to a stochastic transition matrix P by normalizing each row of M to sum to one. We are assuming that the dynamics of the system under the cyclic loading is sufficiently stationary. This is reasonable since transients in macroscopic force measurements only last for the first few compression/decompression cycles²⁰. Since P is a stochastic matrix, its leading eigenvalue is equal to one. The eigenvector associated with this leading eigenvalue provides an estimate of the invariant density, or mass, of the dynamics on the state space²⁷. Its entries essentially correspond to the abundance of states visited by the dynamics, i.e., the most prevalent set of conformations, or set of cycle vectors.

Further transformations of the matrix P can be made. In particular, to identify the sets of states that are most invariant under a *single* time step we can make P time-reversible. This is achieved using the following transformation $R = (P + \hat{P})/2$ where the entries of \hat{P} are $\hat{P}_{ij} = p_j P_{ji}/p_i$ and the p_i are the entries of the eigenvector corresponding to the leading eigenvalue of P ²⁷. That is, R , as constructed above, captures the average transition behaviour of one time step, averaged over the entire loading period. Given reasonable assumptions regarding stationarity, the entries of the second eigenvector of R can be used as the basis of a clustering algorithm to partition the state space into collections of disjoint almost-invariant sets (AI-sets)²⁷. The membership of these AI-sets correspond to states for which inter-member transitions are preferred across one time step. That is, transitions between preferred conformations, or transitions between preferred symbolic cycle vectors are identified. We use the term almost-invariant as there is some leakage between the AI-sets. That is, there is a non-zero probability that states in one AI-set will transition into a state in another AI-set. However, this probability is a lot smaller than the probability a state will transition to another state in the same AI-set as itself.

We can post-process the make-up of these AI-sets at any time slice of the deformation and see which AI-sets hold sway, i.e., which sets contain the most particles during periods of compression or decompression. In this way, we can examine which structures — conformation states or n -cycle topology states — are experimentally observed during compression or decompression in the absence of shear and near absence of friction.

3 Results

3.1 Conformations

The experiment is observed for 1200 time steps consisting of 20 cycles. Initially, the sample is in its least compressed arrangement. At each time step and for each particle we observe which structure, or conformation, it and its contacting particles induce. Furthermore, we record the number of novel con-

formations as time increases. By the end of the experiment we identified 5473 unique conformations as shown in Fig. 6. Most new conformations occurred during the time steps when the sample is being compressed the most. There is a rapid fall-off of novel conformations leading up to the completion of the sixth loading cycle. From then on, only when the sample is close to, or at its most compressed state, are novel conformations discovered. These new conformations only differ from already seen conformations by one or two contacts between a particle's neighbours.

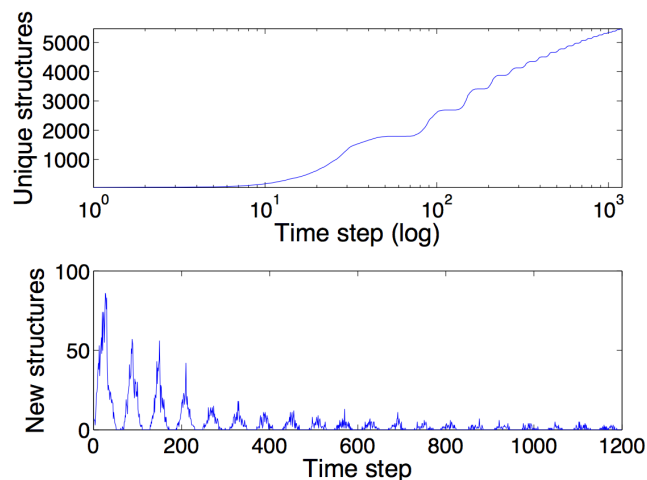


Fig. 6 The number of unique structures/conformations and their discovery through loading.

In terms of the transition dynamics analysis, the 5473 unique conformations define a finite state space of 5473 unique states. We construct a 5473 by 5473 transition matrix by recording for all time intervals of size one time step, the number of times a particle in conformation, or state i , transitions to a conformation, or state j . In Fig. 7 we show a zoomed-in view showing only the first 100 labelled conformation entries of the resulting stochastic transition matrix in a log scale. Outside the scope of this zoomed-in view and as a result of the dimension of the state space, the matrix is less populated with entries, since many states, or conformations, are seldom observed. We have ordered conformations by increasing number of contacts in the conformation sub-network. Two features, other than the diagonal dominance, are apparent from this zoomed-in view: (i) As the number of contacts increases there are relatively fewer transitions between denser sub-networks. This is likely a consequence of the experiment typically spending more time in a weakly jammed configuration. (ii) The “boxed” or “gridded” structure apparent in this zoomed-in view suggests that there are structural or dynamical transition barriers between many conformations¹¹. To relate these barriers to conformation structure, we superimpose

on the plot vertical lines to demarcate the conformation state space according to contact number. We note that there appears to be a correspondence between increasing number of contacts in conformations and the possible transition barriers indicated by the whitespace.

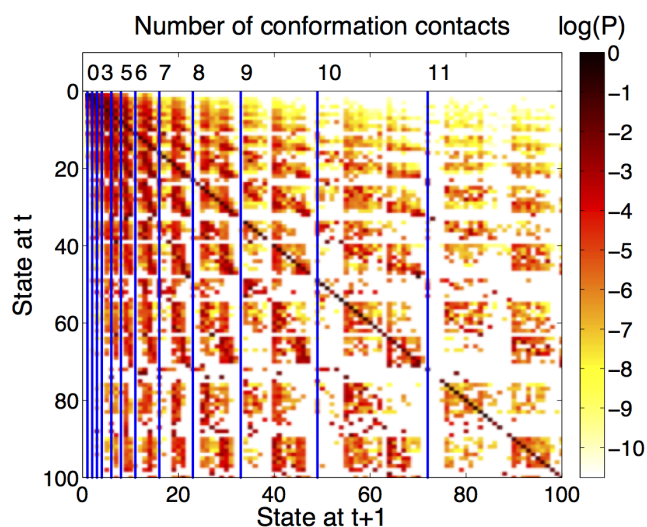


Fig. 7 Conformation state space transition matrix showing the observed transitions (log scale) between the first 100 labelled conformation states. Conformations are ordered by increasing number of contacts in their induced sub-network as indicated by the superimposed vertical lines.

The transition dynamics analysis relies on there being a reasonable relative separation in the eigenvalues of the transition matrix from the leading unity eigenvalue^{11,27}. We found a number of gaps in the eigenspectrum for at least the first half a dozen eigenvalues. Gaps in the eigenspectrum give an indication of the number of AI-sets to determine from the information contained in the corresponding eigenvectors. We use a clustering algorithm to usefully exploit the information contained in the eigenvectors of eigenvalues beyond the largest non-trivial eigenvalue (i.e., the second largest) to better partition the conformation state space into almost-invariant transition sets²⁷. In our calculations we use the right eigenvectors corresponding to the second to sixth largest eigenvalue to partition the conformation state space into five AI-sets, although experience and expertise may decide on different numbers of eigenvalues and AI-sets to be selected.

In Fig. 8 we present the entries of the eigenvector of the unit eigenvalue of the stochastic transition matrix for the first 100 conformations. As before, conformations are labelled by increasing number of contacts. Each conformation is further identified by symbol and colour according to which AI-set they belong to. We see that conformations with the most contacts appear to belong to AI-set number 3, although some of

these larger conformations are identified with AI-sets 4 and 5. The line labelled (probability) “mass” provides information on which conformations are the most prevalent throughout the cyclic loading. The most-prevalent conformations are readily identified. The top six observed conformations — top six peaks in Fig. 8 — are shown in the “Entire” column of Fig. 9, together with the AI-sets in which they are identified. Each conformation shown is labelled to correspond to the labelling convention used in Fig. 8. Also shown in this figure are the top six most prevalent conformations in each AI-set. We note that AI-set number 3 contains the most connected sub-networks and so it is expected that these conformations would be dominant during time steps when the experiment is most compressed and strongly jammed. The most prevalent conformation of AI-set 3 is only the tenth most prevalent conformation. This is again likely due to the experiment spending relatively less time in a strongly jammed state compared to more time in weakly jammed configurations during the decompression sectors of the cyclic loading*. To discount, or observe, any boundary effects with respect to location of prevalent structures, or AI-sets, we also show an empirical density map — xy-projection — of the location of the central particles in the most-prevalent conformations through the *entire* loading history. The left panels of Fig. 9 show the density maps of the adjacent conformation. The bottom panels show the density map of the top six “Entire” conformations and the five AI-sets respectively. Although there appear to be some areas close to the boundaries of the sample where the less-densely connected configurations are preferentially sited there does not appear to a particular bias. We see that AI-set 3, consisting of densely connected conformations, register a high presence throughout the whole sample. Thus boundary effects appear to be minimal.

Once the AI-sets have been identified using observed transitions across the entire loading program, we can post-process their structure, and identify which AI-set of conformations is dominant for each time step, or time slice, of loading. That is, since at a given time each particle is in a unique conformation, we can simply label the particle by the AI-set number its conformation falls in. The number of particles identified to a given AI-set can be calculated for each time step. In Fig. 10 we show these evolving populations. The cyclic nature of the loading causes these traces to repeat, and so only a zoomed-in view is shown for clarity. There is a distinct and consistent pattern in the population of each AI-set. We see that AI-set 3, containing the conformations with the most contacts, encompasses 3/5th’s of the sample during strongly jammed time steps. As the compression is relaxed the number of particles in AI-set 3 falls, with a concomitant rise in the number of particles in AI-sets 2, 5, 1 and 4. From Figs. 9 these sets

*For example, the average degree of the contact networks is above 6 for 44.5% of the time steps, and above 7 for only 14.24%.

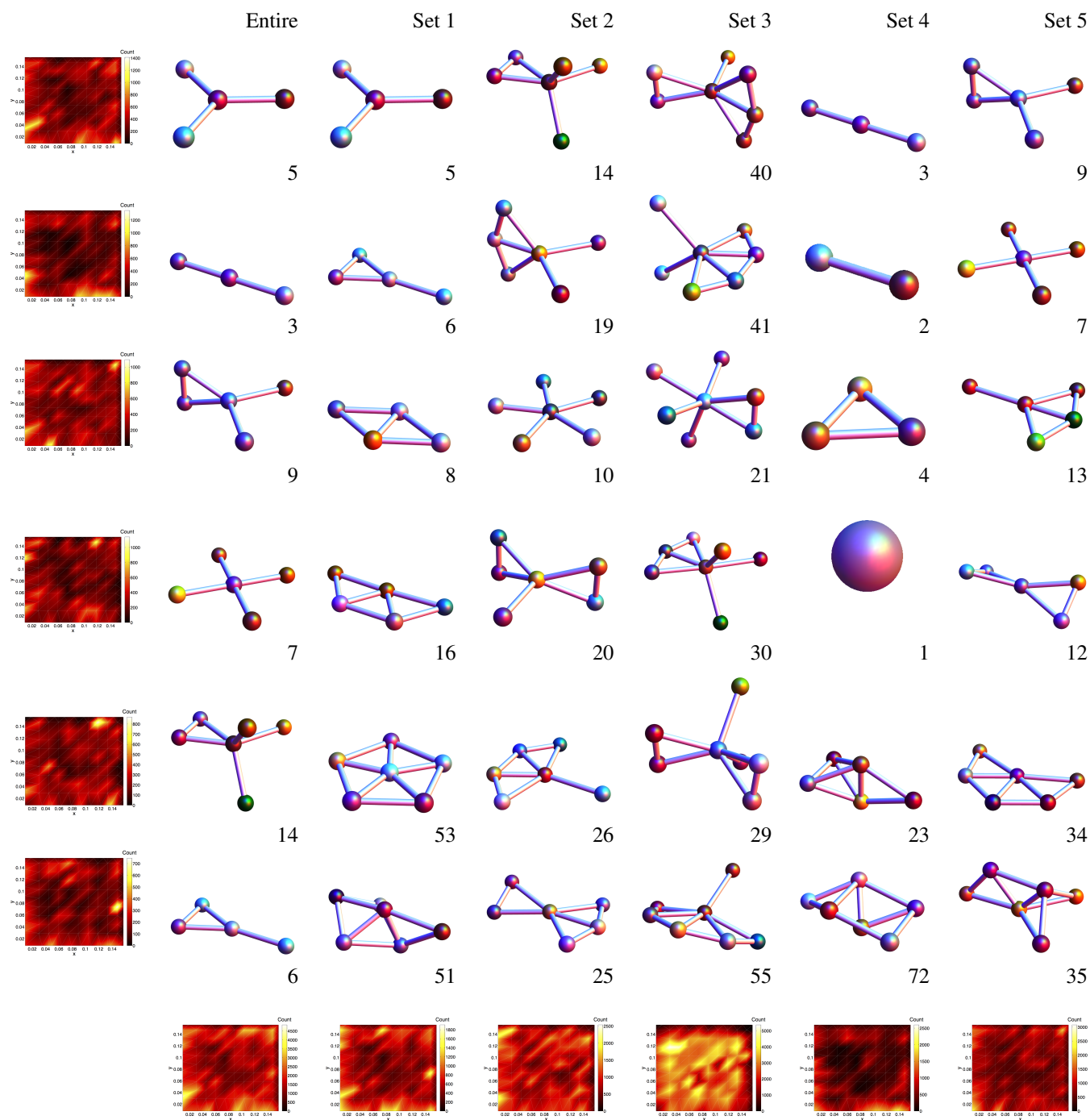


Fig. 9 Sub-networks of the top six most prevalent conformations in each almost-invariant set. Left panels show density maps of the location (xy-projection) of the adjacent most prevalent conformation. The lower panels show density maps of the locations of the top six conformations and the particles in the AI-sets throughout the entire cyclic loading. Boundary affects appear minimal. At the bottom right of each conformation is the label corresponding to its position in Fig. 8.

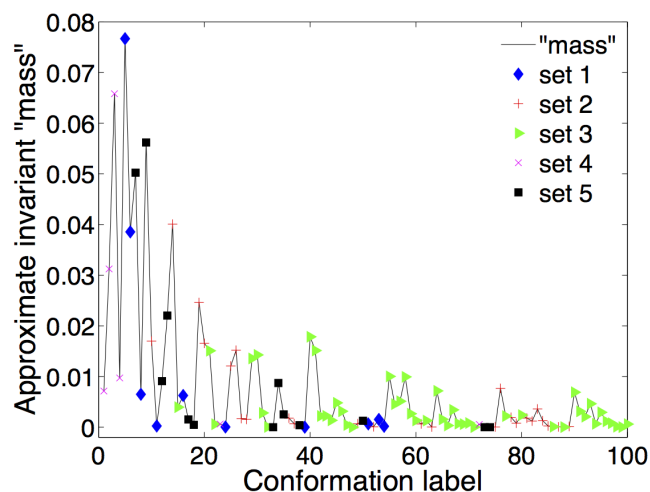


Fig. 8 First 100 labelled conformations and their almost-invariant set membership in conformation state space.

contain a mixture of densely connected sub-networks and less connected sub-networks. During the time steps when the assembly is weakly jammed, the dominant AI-set is set number 4 which contains the sub-networks with the least number of connections. This AI-set still contains a few conformations corresponding to small numbers of tightly packed particles. The 3-cycles present in a few AI-set 4 sub-networks are likely the main contributors to residual stress and support to remnant force chains at these weakly jammed time steps. Recall, the aforementioned experimental limitations regarding undercounting of contacts, and so perhaps this loosely connected AI-set may be even more connected than observed. As compression is once more applied we see the opposite transition dynamics in place: AI-set 3 grows in membership while the population of the other AI-sets falls.

An important set of structures in a load-bearing granular material is the set of force chains⁴¹. These are quasi-linear chains of contacting particles where each particle bears above-average load in the sense of its local particle load vector⁴². For each particle throughout all time steps of the deformation we can classify it as being in the set of force chains or not. This is possible since the experimental setup permits measurements of the contact forces. For the particles identified with force chains we build a histogram of which AI-set their conformation belongs to. In Fig. 11, we present this histogram for the entire cyclic loading programme. We see from this empirical distribution that particles in force chains typically have conformations which sit in AI-set 3. This makes physical sense, since AI-set 3 corresponds to the most densely connected sub-networks and sub-structures with the most contacts. During strongly jammed time steps, the particle population of AI-set 3 is a maximum and the increase in these densely packed sub-

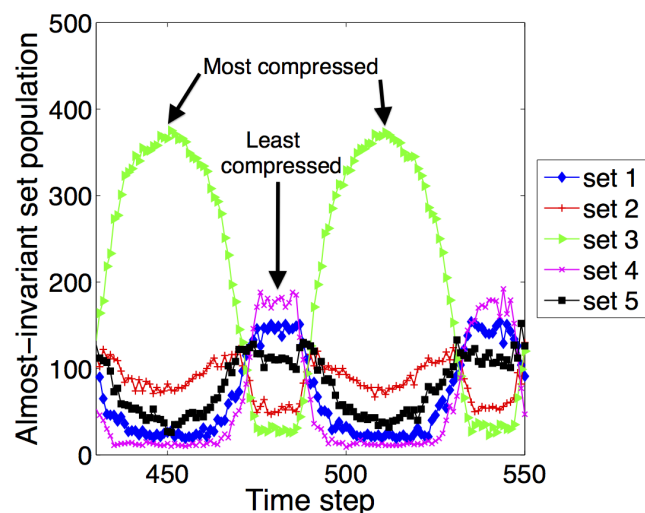


Fig. 10 Zoomed-in view of the almost-invariant set membership of conformation state space through cyclic loading starting at a weakly jammed configuration.

structures clearly promotes the proliferation of force chains among these particles. We note that AI-set 4 associated with the weakly jammed time steps and less well supported sub-structures registers the lowest number of particles forming force chains.

3.2 Cycle vector space

The conformation state space consists of states defined by a particle and its first ring of contacting neighbours. Those conformations are probably the simplest mesoscopic structures to work with analytically¹⁴. However, it has been demonstrated in two dimensions that by considering a slightly larger mesoscopic region, additional insights may be obtained²⁹. This larger mesoscopic domain is achieved by considering a particle and all of the particles included in its local n -cycle topology²⁹. Sub-networks at this scale include the conformation sub-networks as a subset. The increase in scale may lessen the analytic tractability but potentially gives a broader picture of particle rearrangements.

Figure 12 shows an example of a particle's local n -cycle topology. The "central" particle has degree 5, i.e. 5 contacts, and its conformation is the second most prevalent of the conformational AI-set 2, see Fig. 9. Its local minimal n -cycle topology consists of two 3-cycles and two 4-cycles. Its cycle vector is thus $C_i = [0, 2, 2, 0, 0, 0, 0, 0]$ if we set $c_{max} = c_{10}$. Symbolizing gives the cycle state space representation $s_i = [0, 1, 1, 0, 0, 0, 0, 0]$. We can repeat this procedure for all particles at all time steps to determine the set of unique cycle state space representations. We find 256 unique symbolic cycle state space states. Following the same process as

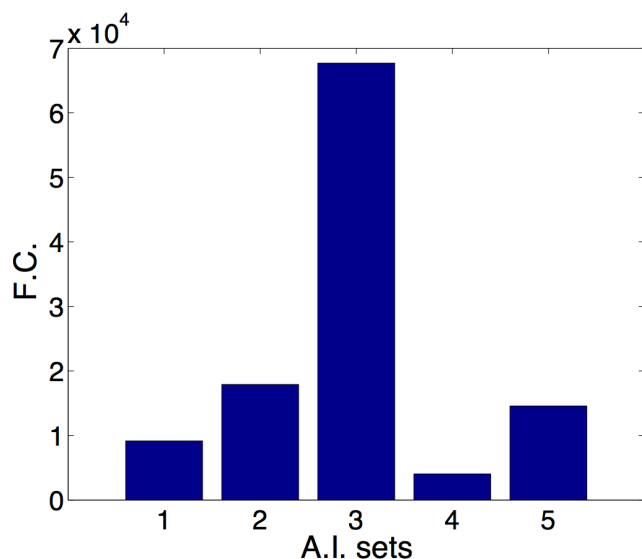


Fig. 11 Conformational almost-invariant (A.I.) set membership of force chain (F.C.) classified particles throughout cyclic loading.

used when analyzing the conformational state space, we build a transition matrix, perform a spectral analysis and determine collections of AI-sets^{11,27}.

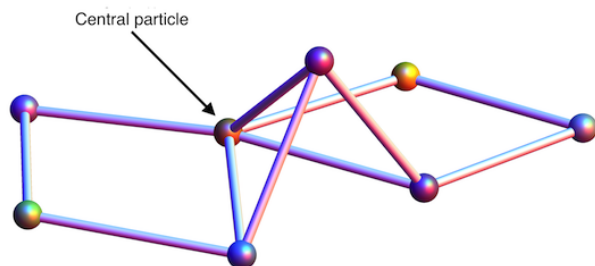


Fig. 12 Induced sub-network of a particle and its n -cycle topology. The central particle is a member of two 3-cycles and two 4-cycles.

The transition matrix in the cycle space is visualized in Fig. 13. Here, the symbolic cycle vector space has been initially ordered by decreasing size according to the size of the smallest n -cycle in the local cycle topology. The superimposed vertical lines demarcate this initial ordering. As was the case for conformations we see a block structure. The diagonal — corresponding to unchanged transitions — appears less dominant in this state space. The eigenvalues of the transition matrix again shows many gaps and a nice spread of values from the leading eigenvalue suggesting that a good partitioning of the state space is possible. As before, we use the eigenvectors of the second to sixth leading eigenvalues of the

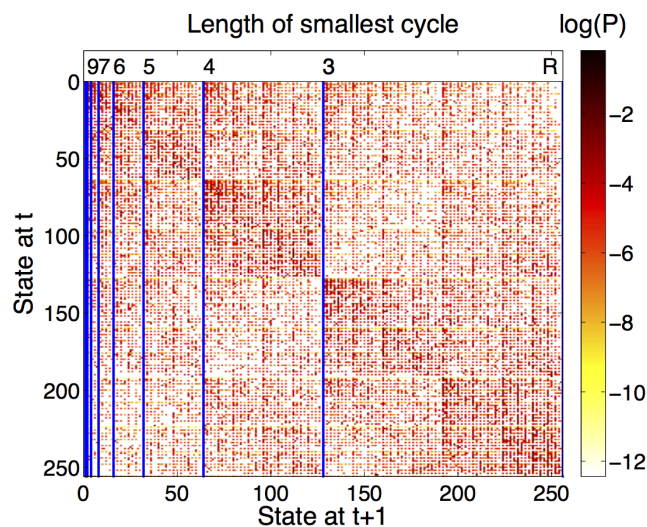


Fig. 13 Observed symbolic cycle vector state space transition (log scale) matrix. Symbolic cycle vectors or particles are initially ordered in decreasing size according to the length of the smallest cycle in the particle's local minimal n -cycle topology. The rattler topology is indicated by "R".

time-reversible transition matrix to perform the partitioning.

The entries of the leading eigenvector of the transition matrix are shown in Fig. 14. The results of the partitioning into AI-sets are shown by colour and symbol. We see that a member of AI-set 1 contains the most prevalent symbolic cycle state. This corresponds to the symbolic cycle vector and structure shown in Fig. 12. The dominant structure of AI-set 4 is state 256 which corresponds to rattler particles. Almost-invariant set 3 contains a lone symbolic cycle space vector, and it corresponds to particles which are solely involved in 3-cycle topologies. In three dimensions, these correspond to isolated clusters of 3-cycles during decompression, or, are particles within closely packed tetrahedral topologies during compression. Examples of sub-structures possessing the dominant symbolic cycle space vector in each AI-set are shown in Fig. 15. These representations are labelled according to symbolic cycle vector consistent with Fig. 14. The dominant cycle vector in AI-set 4 corresponds to the rattler state and is trivially represented by an isolated particle. The next dominant cycle vector in AI-set 4 is non-trivial and corresponds to particles in 8-cycle conformations, for example, see the lower structure in the fourth column of Fig. 15. As was the case for the conformational state space, the top panels show a density map of the location of the central particles of each AI-set member throughout the loading history. There does not appear to be a great bias due to boundary effects, although AI-sets 2, 4 and 5 do show a small preference for boundary site locations.

We can again assign a label to each particle through the

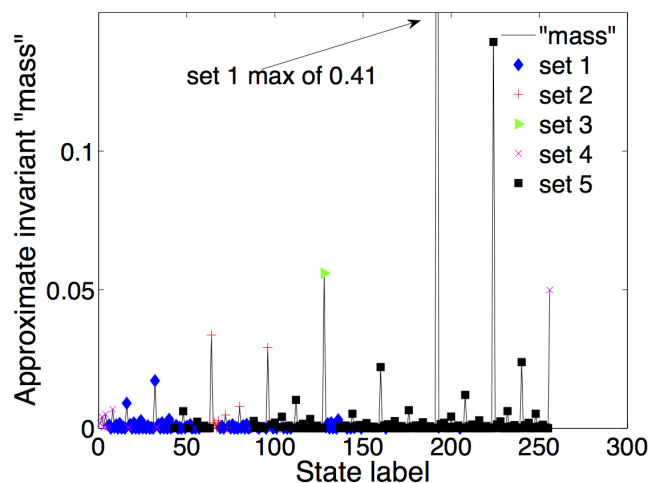


Fig. 14 Almost-invariant set membership of symbolic cycle vector state space.

loading programme according to which AI-set the particle's cycle vector belongs to. Examining Fig. 16, again a zoomed-in view of a cyclical pattern, we see that during periods of strong jamming AI-sets 1 and 3 reach a peak. During periods of weak jamming, the membership of these sets reduce to significantly lower values. Almost-invariant set 1 contains the most dominant structure consisting entirely of 3-cycle and 4-cycle topologies. It makes physical sense that sub-structures with such topologies are the most prevalent (cf. the example of a strongly jammed contact network shown in Fig. 3).

We can investigate the character of the AI-sets further by averaging the entries of the symbolic cycle vectors across cycle size. When we examine the make-up of these almost-invariant sets, we find AI-set 3 consists only of the symbolic 3-cycle representation and its population peaks during periods of strong jamming. Almost-invariant set 1 contains a mixture of 3-cycle topologies and longer cycles. Almost-invariant set 2 rises to a peak during periods of weak jamming and it is noteworthy that its make-up does not include any 3-cycles, but does include 4-cycles in all of its member vectors. Thus when a particle is classified as being in AI-set 2, its local n -cycle topology consists of structures entirely of 4-cycles, or 4-cycles in combinations with longer length cycles. The membership and dynamics of AI-set 5 present a compelling intermediary state. From Fig. 16 we see that its membership reaches a "twin-peak" during the weak jamming phase of loading. The symbolic cycle space vectors consist of all cycles in the same abundance but with a slight bias towards lower length cycles. Recall, the dominant cycle vector across the entire sample resides in AI-set 1 and consists of closely packed sub-structures prevalent during periods of strong jamming. As the material is

decompressed, the population of AI-set 5 increases. Thus the contacts of cycle topologies in AI-set 1 are being broken, resulting in sub-structures with the topologies of AI-set 5. That is, a mixture of tight and loose packing topologies. Since AI-set 5 contains some strongly jammed topologies, these sub-structures become less prevalent as decompression continues: we observe a decrease in the influence of AI-set 5 as the more weakly jammed sets AI-2 and 4 take up the slack. As the compression stage of the cyclic loading recommences, we see a drop in the population of weakly jammed AI-sets 2 and 4, with the "load" now being transferred to AI-set 5. Finally, the system becomes more strongly jammed and AI-set 1 (containing the dominant 3 and 4-cycle combinations) and AI-set 3 (the most densely connected, strongly jammed combinations) take the load. Thus the twin-peak in the population of AI-set 5 is present because its constituent cycle topologies facilitate both off-loading and loading-up stages of the cyclic loading programme.

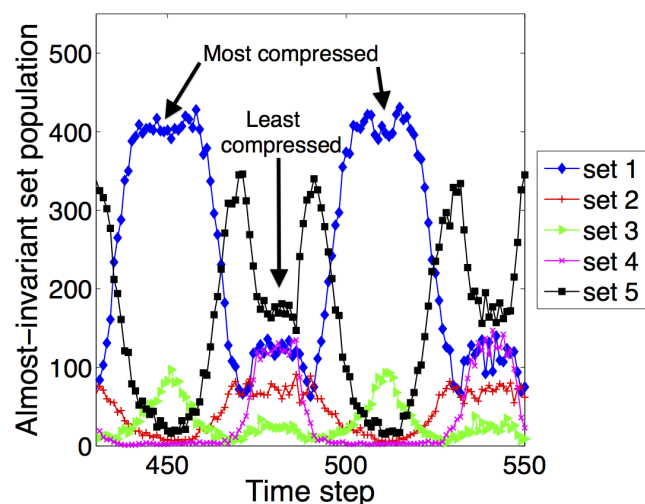


Fig. 16 Zoomed-in view of the particle population in each of the almost-invariant sets through cyclic loading starting from a weakly jammed configuration.

3.3 Roadmaps for deformation and implications for constitutive modelling

One framework for constructing a constitutive law describing the macroscopic stress-strain behaviour of a granular material is the Cosserat continuum. In addition to the equilibrium equations, closure relationships are required to fully determine the unknown components of the generalized stress tensor. Closure relationships can be derived, using a structural mechanics analysis, by explicit consideration of a particular rearrangement event or structural transition. For example, in Tordesillas and Muthuswamy¹⁴, Tordesillas *et al.*³⁰, Torde-

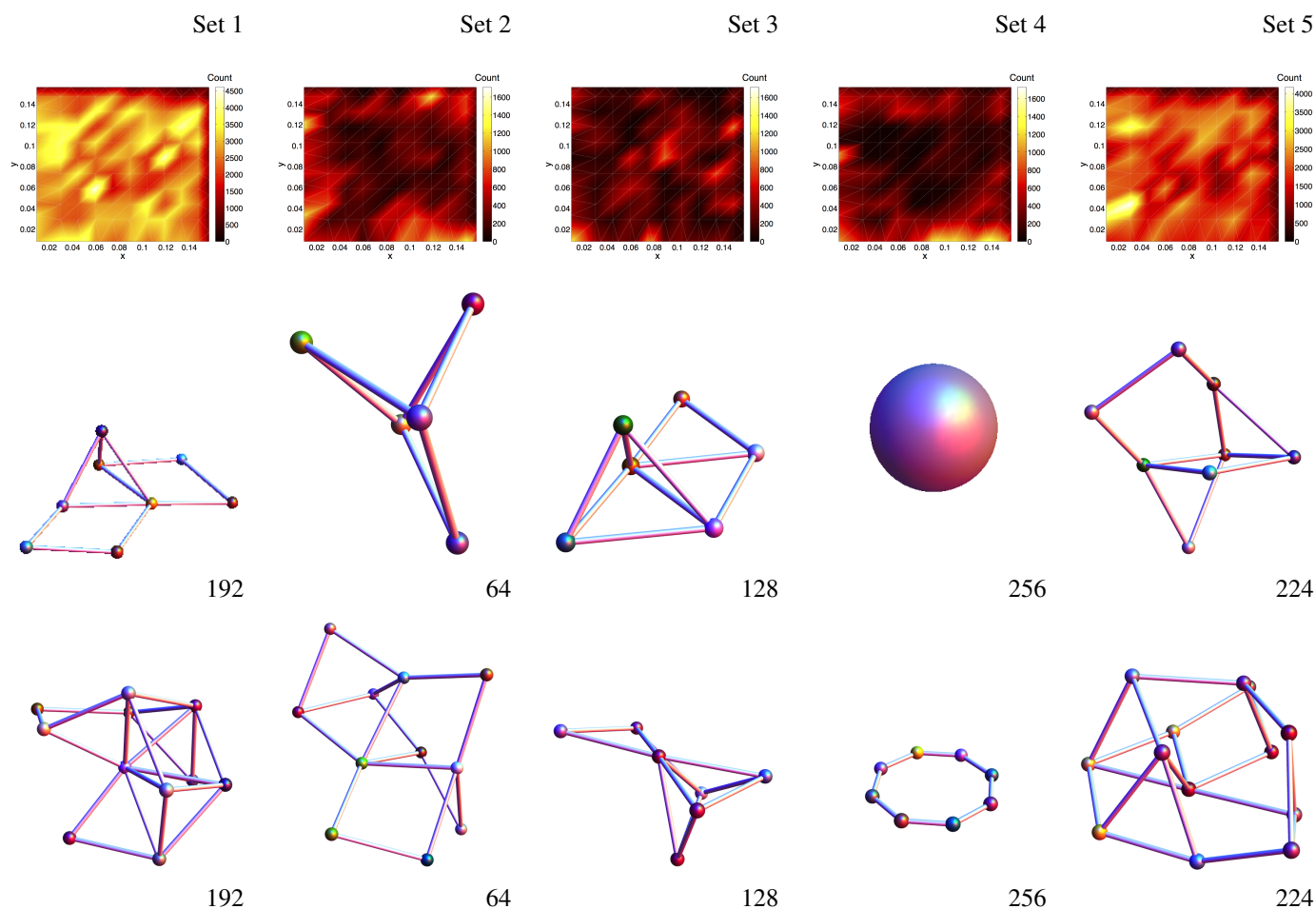


Fig. 15 Examples of sub-structures belonging to the dominant symbolic cycle state space in each almost-invariant set. Top panels show the density throughout loading of the locations (xy -projection) of the central particles in each AI-set. The symbolic cycle vectors of the example structures are: AI-set 1: $s_i = [0, 1, 1, 0, 0, 0, 0, 0, 0]$, AI-set 2: $s_i = [0, 0, 1, 0, 0, 0, 0, 0, 0]$, AI-set 3: $s_i = [0, 1, 0, 0, 0, 0, 0, 0, 0]$, AI-set 4: $s_i = [1, 0, 0, 0, 0, 0, 0, 0, 0]$ and $s_i = [0, 0, 0, 0, 0, 0, 1, 0, 0]$, AI-set 5: $s_i = [0, 1, 1, 1, 0, 0, 0, 0, 0]$. These structures are labelled according to symbolic cycle vector state as per Fig. 14.

sillas and Muthuswamy⁴³, the specific transition corresponded to that presumed to be experienced by a particle and its first ring of neighbours. Specifically, the idealized cluster considered in that study of highly frictional grains embodied a laterally supported three-particle force chain that underwent confined buckling. In Tordesillas and Muthuswamy¹⁴, Tordesillas *et al.*³⁰, Tordesillas and Muthuswamy⁴³, the details of the transition were based on an educated guess, since no information on structural transitions was then available. Indeed in the present study, we can examine the cluster transition pathways in conformational, or cycle vector, space that near-frictionless hydrogel particles follow during a decompression/compression cycle, to propose a sequence of structural transitions that may form the basis for internal variables (e.g. associated nonaffine deformation of the cluster transition) in thermo-micro-mechanical continuum formulations.

Consider a decompression/compression cycle of the deformation and those topologies prevalent at the most compressed state. The evolution of these topologies in the *conformational* state space typically follow AI-sets: $(3) \rightarrow (2) \rightarrow (4) \rightarrow (2) \rightarrow (3)$. For example, Fig. 17 shows one out of many possible conformational transition pathways as the sample is decompressed from a strongly jammed configuration (high degree), through a weakly jammed configuration (low degree), and compressed to return to a strongly jammed configuration. In the figure, the selected conformations are labelled according to Fig. 8. The initial conformation 40 is the most prevalent structure in AI-set 3 (see, Fig. 8 and Fig. 9). The structure selected to represent a transition between AI-sets is the one with highest transition probability: that is, if AI-set 3 conformation 40 transitions to a structure in AI-set 2 then it does so to conformation 19 with the highest transition probability. We note that the transition of conformation 40 to conformation 19 requires the modelling of a dissipative particle rearrangement involving the breaking of two contacts. The specific mechanism is the removal of a triangular support structure. The transition of conformation 19 to conformation 3 suggests an even greater dissipative mechanism, involving loss of three contacts and destruction of two triangles, to be modelled. The reverse process of contact creation, and triangular support forming, occurs during the compression phase of the cycle. In general, a particle in AI-set 3 possesses a structural conformation with many contacting neighbours and many of these neighbours share contacts to form a topology dense in 3-cycles. As the system decompresses to a weakly jammed configuration, these AI-set 3 particles typically form conformations in AI-set 4 via an intermediate collection of conformations typically in AI-set 2: that is, the transition from AI-set 3 to AI-set 2 sees a fall in the number of contacts and a cleaving of 3-cycle support until the prevalent structures of AI-set 4 dominate. These structures include isolated particles, or filamentary chains of particles with very little 3-cycle

support. During compression phases of the cycle, the reverse rearrangements take place, enabling tetrahedral and pyramid structures, comprising 3-cycles and 4-cycles, to self-assemble to form strongly jammed configurations, and allowing the proliferation of force chains. Thus, a roadmap for the deformation of an idealized structure can be followed. With respect to dimensionality, the earlier findings for a two-dimensional system in Tordesillas *et al.*¹¹ appear to similarly apply in three-dimensions: the gain and loss of 3-cycles, here within a variety of 3D structures (e.g., trigonal pyramid, tetrahedron, square pyramid etc.), proved to govern the macroscopic stability and strength of the granular material.

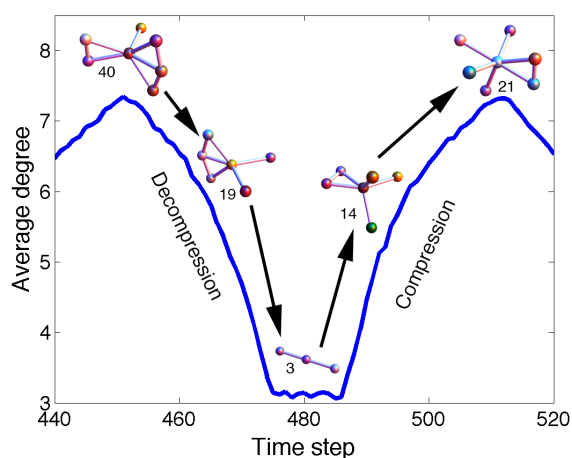


Fig. 17 A proposed transition pathway in conformational space to form the basis for a Cosserat constitutive modelling framework.

Similarly, at the length scale of the *cycle vector* space, if we consider particles in AI-set 3 when the system is at its most compressed, then we typically find the following transition pathway: $(3) \rightarrow (1) \rightarrow (5) \rightarrow (4) \rightarrow (5) \rightarrow (1) \rightarrow (3)$. In this case, an idealized continuum model building block structure would consist of a collection of tetrahedra sharing faces (recall, AI-set 3 consists solely of 3-cycles). During decompression, 3-cycles open up to form 4-cycles and longer length cycles. Particles in AI-set 3 gradually transfer membership to AI-set 1 and AI-set 5, where they form pyramids and larger prisms. These mixed topologies, found in individual mesoscopic structures in this intermediary AI-set, permit the material to efficiently switch from a strongly jammed to a weakly jammed-unjammed macroscopic state during repetitive compression and decompression. When the system is at its most decompressed, and weakly jammed, the particles form structures prevalent in AI-set 4. These structures exhibit a complete absence of 3 and 4-cycles, typically consisting of isolated particles, or long necklaces of particles. The compression phase of the cyclic loading reverses these rearrangement processes

and returns the system particles to densely packed arrangements of tetrahedra. One such transition pathway out of the many possible is shown in Fig. 18. The selected structures are representations of the symbolic cycle vector as labelled in Fig. 14. As per Fig. 17, the selected cycle vector at a transition are those corresponding to highest transition probability. The curve demonstrating the decompression/compression phases of the cycle corresponds to the average clustering coefficient of the assembly. This provides an indication of the loss, and gain, of triangular structures that hydrogel particles participate in during a deformation cycle. We note that for this specific pathway, the change in the number of nodes between the structures is 0, 1, or 2. The greatest change occurs during the initial decompression and final compression phases of the cycle. Thus the length scale of the cycle vector structures may be applicable for uncovering cluster transitions where minimal energy transitions involving the least change in constituent components is desired. Furthermore, we note that the cycle vector space roadmap complements the proposed conformational space roadmap as it informs micromechanical modellers of plausible deformation pathways of particle clusters at larger spatial length scales.

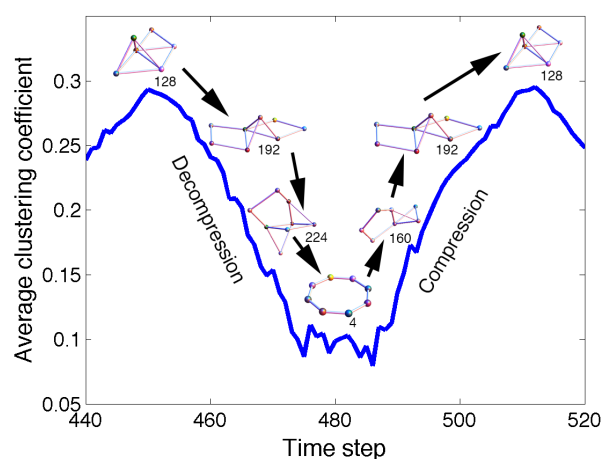


Fig. 18 A proposed transition pathway in cycle vector space to form the basis for a Cosserat constitutive modelling framework. This pathway has a near constant number of constituent particles despite the significant re-configurations.

4 Conclusion

We have explored self-assembly by examining structures and structural transitions that emerge within a three-dimensional granular material when its macroscopic mechanical state is changing from weakly to strongly jammed. The experimental test system is unique in that the sample deformed under

conditions that were free from the major influences of friction and grain shape — two key factors known to govern structural self-assembly in dense granular media. This was achieved by studying a three-dimensional granular material comprising hydrogel beads that was uniaxially compressed and decompressed in a cyclic loading protocol. The experimental apparatus under this loading protocol was capable of driving the material backwards and forwards between weakly and strongly jammed states. The ability to observe the structural topology of the material across many cycles allows a robust statistical and dynamical analysis of internal structures inherent in this three-dimensional system, within the framework of a Markov transition dynamics analysis.

In summary, we examined the structures and structural transitions that meso-scale clusters of particles self-assemble into within two structural state spaces — at the highest temporal length scale of observation possible for this experiment (across a time-scale of one strain step). In the first state space, the spatial scale is that spanned by a particle and its first ring of contacting neighbours: this structure defines the conformational state space. In the second state space, multiple spatial scales are spanned by a particle and its minimal cycle topology: this structure defines a cycle vector state space. In each state space, a collection of almost-invariant transition sets were discovered that compellingly describe the structural evolution of the system, as it cycles between being globally strongly jammed and globally weakly jammed. These observations are of importance to thermo-micro-mechanical constitutive formulations where starting points are to model structural deformation at the mesoscopic scale, and then to use this process as the building block for macroscopic averaging to the continuum from internal variables (e.g., non-affine deformation¹⁴ and damage-healing from loss-gain of contacts within mesoscopic structures¹⁵). As such, we were able to postulate two transition pathways and mechanisms to broadly motivate a Cosserat modelling framework for a densely packed granular system near the frictionless limit. This also opens the door for a similar analysis to be undertaken for other physical systems (e.g. sand) with higher grain-grain contact friction — a factor known to stabilise contacts and, in turn, the build-up of force, stored energy and stable force chains. A program of research that explores this aspect is ongoing which, in addition to friction, will address the effects of grain shape on structural transition pathways. Finally, above and beyond the direct implications for constitutive modelling of granular materials, we envisage potential utility of the findings and methods of this study in the design of additives to strengthen granular materials, or to enhance particular aspects of granular behaviour (e.g., flowability, ability to switch efficiently to a compacted state) especially under repetitive loading conditions (e.g., road and off-road construction materials, pavement), and in the design of novel granular materials with tailor-made properties

(e.g., 3D printed particulate systems).

Acknowledgments

This work was supported by US Army Research Office (W911NF-11-1-0175, W911NF-1-11-0110), the Australian Research Council Discovery Projects 2012 (DP120104759) and a Future Fellowship (FT120100025), NASA grant (NNX10AU01G), NSF grant (DMR12-06351), the W. M. Keck Foundation and the Melbourne Energy Institute.

References

- 1 J. Duran, *Sands, Powders, and Grains: An Introduction to the Physics of Granular Media*, Springer-Verlag, New York, 2000.
- 2 P. Radziszewski, *Minerals Engineering*, 2013, **46–47**, 83–88.
- 3 M. Z. Miskin and H. M. Jaeger, *Soft Matter*, 2014, **10**, 3708–3715.
- 4 S. Roshankhah and J. C. Santamarina, *Geotechnique Letters*, 2014, **4**, 145–150.
- 5 H. Zhu, Z. Zhou, R. Yang and A. Yu, *Chemical Engineering Science*, 2008, **63**, 5728–5770.
- 6 J. Paavilainen and J. Tuhkuri, *Cold Regions Science and Technology*, 2013, **85**, 157–174.
- 7 J. Estep and J. Dufek, *Journal of Volcanology and Geothermal Research*, 2013, **254**, 108–117.
- 8 Self-organizing systems: 6th IFIP TC 6 International Workshop, Delft, The Netherlands, 2012.
- 9 A. Tordesillas, Q. Lin, J. Zhang, R. P. Behringer and J. Shi, *J. Mech. Phys. Solids*, 2011, **59**, 265–296.
- 10 A. Tordesillas, D. M. Walker, E. Andò and G. Viggiani, *Proceedings of the Royal Society A*, 2013, **469**, 201220606.
- 11 A. Tordesillas, D. M. Walker, G. Froyland, J. Zhang and R. P. Behringer, *Phys. Rev. E*, 2012, **86**, 011306.
- 12 A. J. Liu and S. R. Nagel, *Nature*, 1998, **396**, 21–22.
- 13 D. Bi, J. Zhang, B. Chakraborty and R. P. Behringer, *Nature*, 2011, **480**, 355–358.
- 14 A. Tordesillas and M. Muthuswamy, *J. Mech. Phys. Solids*, 2009, **57**, 706–727.
- 15 X. K. Li, Y. Y. Du and Q. L. Duan, *Int. J. Damage Mech.*, 2013, **22**, 643–682.
- 16 L. Chai, X. Wu and C. S. Liu, *Soft Matter*, 2014, **10**, 6614–6618.
- 17 E. Azéma, N. Estrada and F. Radjai, *Physical Review E*, 2012, **86**, 041301.
- 18 F. Radjai, J.-Y. Delenne, E. Azéma and S. Roux, *Granular Matter*, 2012, **14**, 259–264.
- 19 S. Wegner, R. Stannarius, A. Boese, G. Rose, B. Szabó, E. Somfai and T. Börzsönyi, *Soft Matter*, 2014, **10**, 5157–5167.
- 20 N. Brodu, J. A. Dijksman and R. P. Behringer, *Spanning the scales of granular materials: microscopic force imaging*, *Science*, submitted, 2014.
- 21 J. A. Dijksman, H. Zheng and R. P. Behringer, *Powders and Grains 2013: AIP Conf. Proc.*, 2013, **1542**, 457.
- 22 C. S. O'Hern, S. A. Langer, A. J. Liu and S. R. Nagel, *Phys. Rev. Lett.*, 2002, **88**, 075507.
- 23 N. Xu and C. S. O'Hern, *Phys. Rev. E*, 2006, **73**, 061303.
- 24 G.-J. Gao, J. Blawdziewicz and C. S. O'Hern, *Philos. Mag.*, 2007, **87**, 425–431.
- 25 C. F. Schreck, C. S. O'Hern and L. E. Silbert, *Phys. Rev. E*, 2011, **84**, 011305.
- 26 C. Reichhardt and C. J. O. Reichhardt, *Soft Matter*, 2014, **10**, 2932–2944.
- 27 G. Froyland, *Physica D*, 2005, **200**, 205–219.
- 28 J. Zhang, T. Majmudar, A. Tordesillas and R. P. Behringer, *Granular Matter*, 2010, **12**, 159–172.
- 29 D. M. Walker, A. Tordesillas and G. Froyland, *Phys. Rev. E*, 2014, **89**, 032205.
- 30 A. Tordesillas, J. Shi and J. F. Peters, *Granul. Matter*, 2012, **14**, 295–301.
- 31 T. Lachhab and C. Weill, *Eur. Phys. J. B*, 1999, **9**, 59–69.
- 32 S. Mukhopadhyay and G. Peixinho, *Phys. Rev. E*, 2011, **84**, 011302.
- 33 J. A. Dijksman, F. Rietz, K. A. Lorincz, M. van Hecke and W. Losert, *Rev. Sci. Instrum.*, 2012, **83**, 011301.
- 34 K. Lorincz and P. Schall, *Soft Matter*, 2010, **6**, 3044–3049.
- 35 A. Smart and J. M. Ottino, *Soft Matter*, 2008, **4**, 2125–2131.
- 36 D. M. Walker and A. Tordesillas, *Int. J. Solids Struct.*, 2010, **47**, 624–639.
- 37 M. E. J. Newman, *Networks: An Introduction*, Oxford University Press, Great Clarendon Street, Oxford, 2010.
- 38 N. W. Johnson, *Canadian J. Math.*, 1966, **18**, 169–200.
- 39 J. D. Horton, *SIAM J. Computing*, 1987, **16**, 358–366.
- 40 K. Mehlhorn and D. Michail, *ACM J. Experimental Algorithmics*, 2006, **11**, 1–14.
- 41 J. F. Peters, M. Muthuswamy, J. Wibowo and A. Tordesillas, *Phys. Rev. E*, 2005, **72**, 041307.
- 42 M. Muthuswamy and A. Tordesillas, *J. Stat. Mech. Theory Exp.*, 2006, **P09003**.
- 43 A. Tordesillas and M. Muthuswamy, *Acta Geotechnica*, 2008, **3**, 225–240.